Daket *et al. Earth, Planets and Space* (2016) 68:157
DOI 10.1186/s40623-016-0531-0

Earth, Planets and Space

FULL PAPER Open Access

Tectonic evolution of northwestern Imbrium of the Moon that lasted in the Copernican Period

Yuko Daket[1*], Atsushi Yamaji[1], Katsushi Sato[1], Junichi Haruyama[2], Tomokatsu Morota[3], Makiko Ohtake[2] and Tsuneo Matsunaga[4]

Abstract

The formation ages of tectonic structures and their spatial distributions were studied in the northwestern Imbrium and Sinus Iridum regions using images obtained by Terrain Camera and Multiband Imager on board the SELENE spacecraft and the images obtained by Narrow Angle Camera on board LRO. The formation ages of mare ridges are constrained by the depositional ages of mare basalts, which are either deformed or dammed by the ridges. For this purpose, we defined stratigraphic units and determined their depositional ages by crater counting. The degradation levels of craters dislocated by tectonic structures were also used to determine the youngest limits of the ages of the tectonic activities. As a result, it was found that the contractions to form mare ridges lasted long after the deposition of the majority of the mare basalts. There are mare ridges that were tectonically active even in the Copernican Period. Those young structures are inconsistent with the mascon tectonics hypothesis, which attributes tectonic deformations to the subsidence of voluminous basaltic fills. The global cooling or the cooling of the Procellarum KREEP Terrane region seems to be responsible for them. In addition, we found a graben that was active after the Eratosthenian Period. It suggests that the global or regional cooling has a stress level low enough to allow the local extensional tectonics.

Keywords: Moon, SELENE (Kaguya), Mare Imbrium, Geohistory, Copernican tectonics, Contraction, Extension

Introduction

Mare ridges and straight rilles are map-scale tectonic features on the Moon. They are interpreted as compressional and extensional tectonic structures, respectively (e.g., Bryan 1973; Gilbert 1893; Howard and Muehlberger 1973; Maxwell et al. 1975). The roughly concentric and radial patterns made by the features with respect to the centers of the mascon basins (Fig. 1) have been thought to suggest the subsidence of massive mare fills as their origins (Baldwin 1968; Brennan 1976; Maxwell et al. 1975; Wilhelms and McCauley 1971). The loading is expected to have led to more or less syndepositional tectonics (Solomon and Head 1979); that is, the tectonic deformations should be mainly of the Imbrian and early Eratosthenian, because the mare volcanism to fill the basins climaxed in the periods (e.g., Hiesinger et al. 2000; Morota et al. 2011).

However, recent discoveries of young tectonic features by the SELenological and ENgineering Explorer (SELENE) project (Ono et al. 2009) and the Lunar Reconnaissance Orbiter Camera (LROC) (Watters et al. 2010) question the mascon loading hypothesis. The timing of the tectonic deformations is important for determining their origins. There are mechanisms that can explain young tectonism, including global cooling (Solomon and Chaiken 1976; Pritchard and Stevenson 2000) and the orbital evolution of the Earth–Moon system (Melosh 1980).

This work is devoted to evaluating the formation ages of tectonic structures in northwestern Imbrium (Figs. 1, 2). The Imbrium basin is a typical mascon basin with concentric mare ridges and is located within Procellarum KREEP

*Correspondence: yukodakeko@gmail.com
[1] Division of Earth and Planetary Science, Kyoto University, Kyoto, Japan
Full list of author information is available at the end of the article

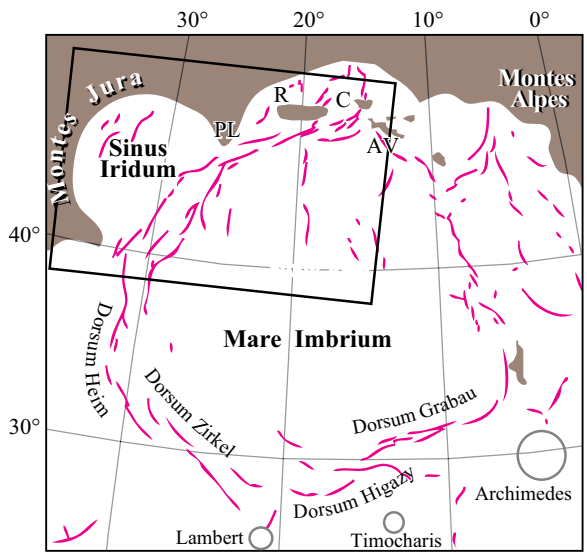

Fig. 1 Concentric systems of the mare ridges in Mare Imbrium. *Red lines* indicate the mare ridges, *gray circles* indicate prominent craters, and *brown areas* indicate highland materials. PL: Promontorium Laplace. R: Montes Recti. C: Mons Chajorra. AV: Alta Vista

Terrane (PKT). The basin has surfaces with various crater ages and has a candidate landing site for future missions (e.g., Qiu and Stone 2013). In order to evaluate the formation ages, we first defined the mare units based on spectral features. Second, we made crater size–frequency distribution (CSFD) measurements of the units and determined their depositional ages. Finally, the timing of the tectonic deformations was constrained based on the crosscutting relationships between tectonic structures and the mare units. The degradation levels of small craters (Moore et al. 1980) affected by thrust faults were also used to estimate the timing of the youngest tectonic activity.

Data

We mainly used the images and spectral data taken by the Terrain Camera (TC) and Multiband Imager (MI) onboard the SELENE spacecraft (Haruyama et al. 2008; Kato et al. 2010; Ohtake et al. 2008). They uniformly cover the entire lunar surface. The TC images have an average spatial resolution of ~10 m and relatively low solar elevation angles of ~20°, which is advantageous to crater counting and observing low-relief topographic features (Haruyama et al. 2008). The digital terrain models (DTM) produced from the stereo pairs of TC images have horizontal and vertical resolutions of ~10 m (Haruyama et al. 2008). The DTMs describe altitudes from the spherical surface with a radius of 1737.4 km. In order to screen out the long-wavelength topography and to enhance short-wavelength tectonic topography, the present selenoid was subtracted from the DTMs. The selenoid is determined by the gravity model of degree 660 in the spherical harmonics obtained by the Gravity Recovery and Interior Laboratory (GRAIL) (Lemonie et al. 2013). The MI obtained spectral data at four visible and five near-infrared spectral bands with spatial resolutions of 20 and 60 m, respectively (Ohtake et al. 2008). We used the near-infrared spectral data of the MI_MAP product that had been converted into reflectance of the lunar surface by Ohtake et al. (2010).

We used high-resolution images taken by the Lunar Reconnaissance Orbiter Camera (LROC) Narrow Angle Cameras (NACs) as well to observe the crosscutting relationships of craters and tectonic features. Those images have a spatial resolution of 0.5–2 m (Robinson et al. 2010).

Stratigraphic units and their ages

We used the differences in spectral features to define the mare units and conducted the CSFD measurements on each unit.

Stratigraphic units

We defined the stratigraphic mare units in the study area based on the spectral ratio images made from the MI images at 414, 749 and 950 nm wavelengths. The spectral bands were chosen to enhance the contrasts in maturity, Ti content and Fe content of the basalts (Fischer and Pieters 1994; Lucey et al. 1995; Pieters et al. 1980). Figure 2c shows a mosaic of spectral ratio images, where relatively mature or low-Ti mare basalts are indicated by purplish or reddish colors and immature, high-Ti or high-Fe basalts by bluish ones. The circular yellowish spots indicate fresh craters and their ejecta blankets in this image.

We defined nine units from A through I. The spectral ratio image shows that the mare in the study area is clearly divided into two regions with warm and cold colors (Fig. 2c). This contrast has long been recognized since the Apollo era (e.g., Whitaker 1972; Pieters 1978). The bluish area is named Unit E, whereas the remaining reddish areas were subdivided into Units A through D and F through I. The southern border of Unit F and the eastern border of Unit H are not clear because the spectral features gradually change. The hatched areas in Fig. 2c have spectral features distinctive from those of the neighboring units, but the CSFD measurement was hampered by abundant secondary craters or the small areal extent.

Several researchers made CSFD measurements in our study area (e.g., Bugiolacchi and Guest 2008; Hiesinger et al. 2000; Morota et al. 2011; Thiessen et al. 2014). They used Galileo, Clementine, Chandrayaan-1 and Lunar Orbiter images to define the mare units. Their divisions

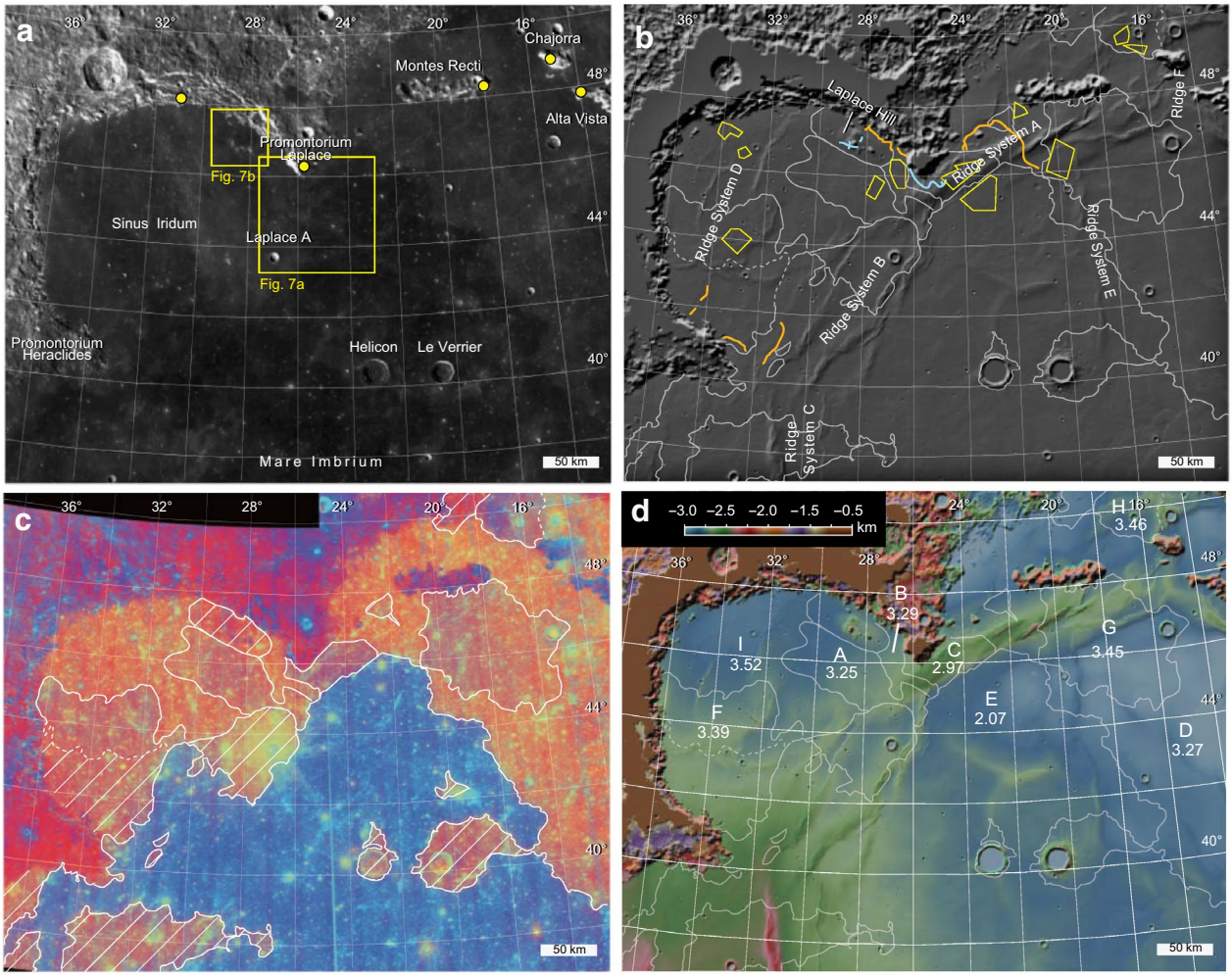

Fig. 2 Images of the study area taken by SELENE. **a** TC images. *Yellow spots* indicate the locations of lobate scarps. **b** Embossed image of grayscale image of the digital terrain model (DTM) made by Haruyama et al. (2008) from SELENE data. Highland with the altitudes above −1000 m is out of range to highlight low-relief topographic features in the mare. *Orange* and *blue lines* indicate grabens and sinuous rilles, respectively. *Yellow boxes* indicate the areas where CSFD measurements were taken. **c** Spectral ratio images shown in *false color* (749/414 nm on *red*, 749/950 nm on *green*, 414/749 nm on *blue*) with the mare units defined in this study. **d** Topography overlaid with the embossed image shown in **b**. Crater ages of the units in Ga are indicated as well

coincide with ours more or less, except for units in Sinus Iridum. The surface of the bay can be subdivided into several units, but it is difficult to trace their boundaries due to the low contrasts in spectral features and to the NNW trending ray with a width of 20 km (Fig. 2a, c). As a result, the division of the mare units by Hiesinger et al. (2000), Bugiolacchi and Guest (2008), Thiessen et al. (2014) and this study is different in the bay. We used the uniform and high-resolution MI images of this region and divided the bay into seven units. The images have higher resolution than the data set used by the previous studies. The discrepancy between our results and previous results might be induced by the differences in the spatial resolution and/or in the wavelength of the spectral data. Among the seven units, three (hatched areas in Fig. 2c) have such abundant secondary craters that their depositional ages could not be determined.

Crater ages of stratigraphic units

The CSFD measurement was taken in the portion of the region where secondary craters are few in each mare unit. The lambert azimuthal equal-area projections of the TC images were used for crater counting to measure the surface area accurately. We used the production and chronology functions proposed by Neukum (1983) and Neukum et al. (2001). The former is expressed as

$$\log_{10} N(D) = a_0 + \sum_{n=1}^{11} a_n (\log_{10} D)^n, \quad (1)$$

where D is the diameter of the craters in kilometers, $N(D)$ is the cumulative number density of craters larger than D per km^2, and the coefficients from a_1 through a_{11} are the constants, the values of which are given by Ivanov et al. (2001) and Neukum et al. (2001) for the craters satisfying $0.1 < D < 200$ km. The coefficient a_0 is age dependent. This value is given by fitting the production function (Eq. 1) to the observed CSFD. The model age of a unit in Ga, T, is obtained according to the chronology function (Neukum 1983), $N(1) = 5.44 \times 10^{-14}[\exp(6.93T) - 1] + 8.38 \times 10^{-4}T$, where $N(1) = 10^{a_0}$ (Eq. 1).

We estimated the ages of Units A through I (Table 1; Fig. 2d). Figure 3 shows the CSFDs in the units. We carefully drew the boundaries of the crater counting areas in the mare units to exclude portions with steep slopes or abundant secondary craters. As a result, the model ages of Units I, H and G were estimated as 3.52, 3.46 and 3.45 Ga, respectively. Unit F was 3.39 Ga. Units B, D and A were 3.29, 3.27 and 3.25 Ga. Unit C was 2.97 Ga. The youngest unit, Unit E, was estimated as 2.07 Ga. The production function was fitted to the distributions for the craters with D between 0.25 and 1 km following Morota et al. (2011). The upper limit of D is determined from the fact that there are few craters larger than 1 km in the counting areas. Considering the confidence intervals, the ages of the mare units determined in previous studies (Hiesinger et al. 2000; Bugiolacchi and Guest 2008; Qiao et al. 2014) are roughly consistent with our results except for Units E, F, H and I (Fig. 4).

Table 1 Model ages of investigated mare units in northern Imbrium

	Area (km^2)	N	$N(1)$ (10^{-3} km^{-2})	Model age (Ga)	
Unit A	135	57	3.05	3.25	+0.10 −0.19
Unit B	254	129	3.20	3.29	+0.06 −0.09
Unit C	274	116	2.53	2.97	+0.16 −0.23
Unit D	220	103	3.11	3.27	+0.07 −0.12
Unit E	530	150	1.73	2.07	+0.17 −0.17
Unit F	294	154	3.74	3.39	+0.04 −0.05
Unit G	397	207	4.21	3.45	+0.03 −0.03
Unit H	251	143	4.32	3.46	+0.03 −0.04
Unit I	263	194	5.05	3.52	+0.02 −0.03

N indicates the numbers of craters counted larger than 1 km in diameter. $N(1)$ is the density of craters with diameters larger than 1 km. Model ages are quoted at the 1 sigma error level

The discrepancies in the age of Unit E can be explained by the differences in the ranges of crater sizes targeted in the CSFD measurements. Our result is consistent with Morota et al. (2011) and Bugiolacchi and Guest (2008), but not with Hiesinger et al. (2000) and Qiao et al. (2014). We counted craters larger than 250 m in diameter, a few times smaller than the threshold used by the previous studies. Hiesinger et al. (2000) used craters larger than 800 m in diameter to use the Lunar Orbiter IV images, which have a spatial resolution of 60–150 m. Bugiolacchi and Guest (2008) also used these images, but they counted craters larger than 500 m instead of 800 m. Qiao et al. (2014) counted craters larger than 500 m with LROC wide angle camera images, which have resolution of ~100 m. Small craters are easily obliterated by thin and younger lavas, but larger craters with high rims are not. The rim heights of 20 and 30 m correspond to the crater diameters of 500 and 800 m, respectively (Pike 1977, p. 88), which Hiesinger et al. (2000), Qiao et al. (2014) and Bugiolacchi and Guest (2008) used as the minimal crater in the CSFD measurements. Accordingly, the number densities of smaller and larger craters tend to indicate younger and older ages, respectively, if smaller ones have been obliterated by younger lavas. Therefore, an obliteration by lavas with a total thickness of several tens of meters explains the older age in Hiesinger et al. (2000) and Qiao et al. (2014). Since craters larger than 500 m were rare in our counting areas, the obliteration did not appear as a jump in the CSFD plot in Fig. 3. Secondary craters in Unit E were infrequent and were distinctive from primary craters.

We counted a larger number of craters and used higher-resolution and lower solar angle images, which advantageous to crater counting, than the previous studies (Bugiolacchi and Guest 2008; Hiesinger et al. 2000; Qiao et al. 2014). Therefore, though the results of the estimated ages of Units F, H and I disagree with the previous studies (Bugiolacchi and Guest 2008; Hiesinger et al. 2000), we adopt our results. However, many secondary craters were observed in Units F, H and I. We carefully excluded them, but possibly made an overestimation of the ages owing to their contamination.

Tectonic features and formation ages

There are a number of mare ridges, grabens and lobate scarps in the study area, which we describe in the following subsections. We constrained the formation ages of the ridges by the ages of the mare units dammed and deformed by the ridges. Since the mare basalts were so

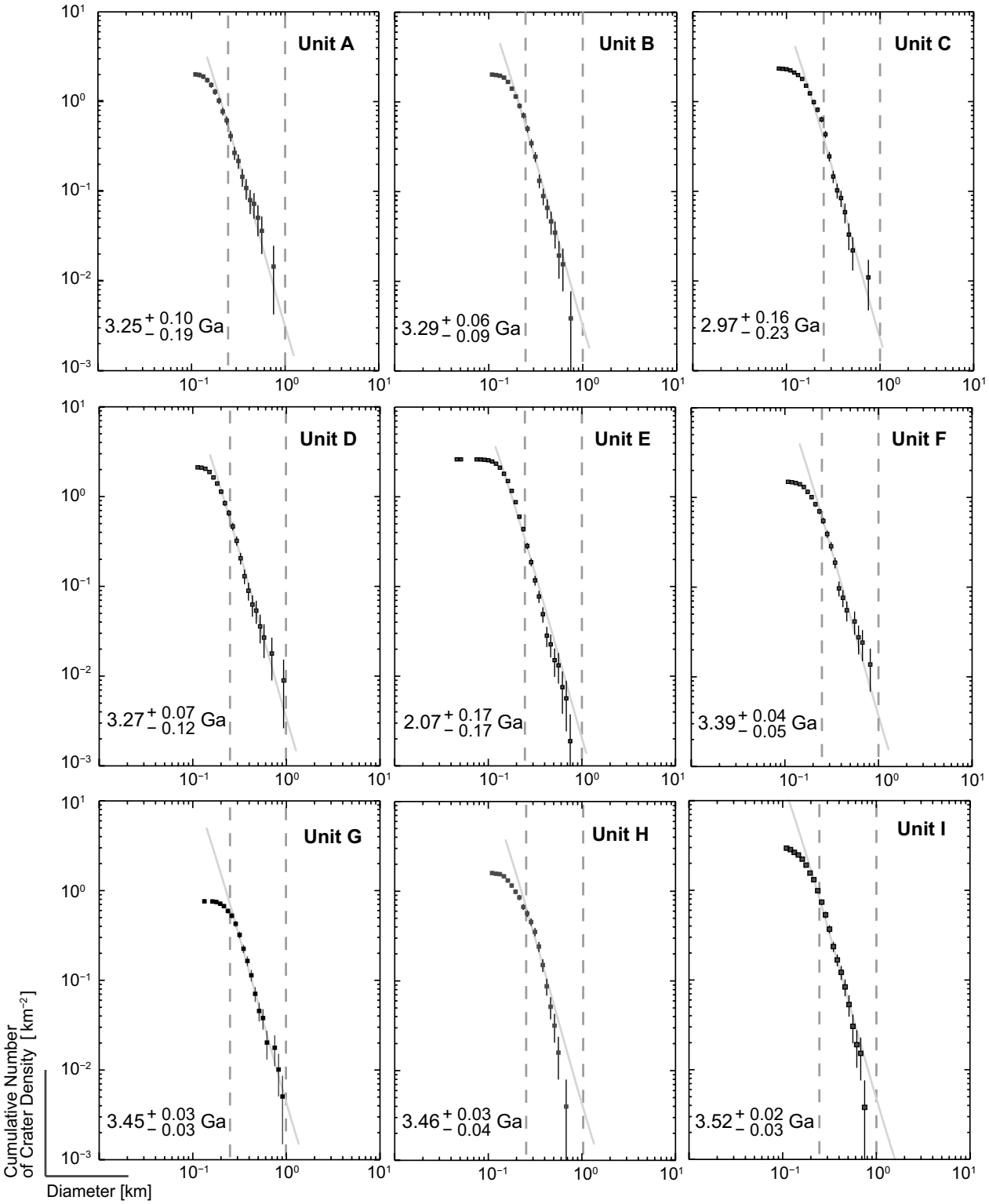

Fig. 3 The CSFDs for the units. Craters 250–1000 m in diameter were used. *Dashed lines* indicate the diameter ranges used to fit the production function. The *error bars* are calculated by $\log(N \pm N^{1/2}) / A$, where N is the cumulative number of craters and A is the counted area. The CSFDs are for *Units A*, *B*, *C*, *D*, *E* and *F*

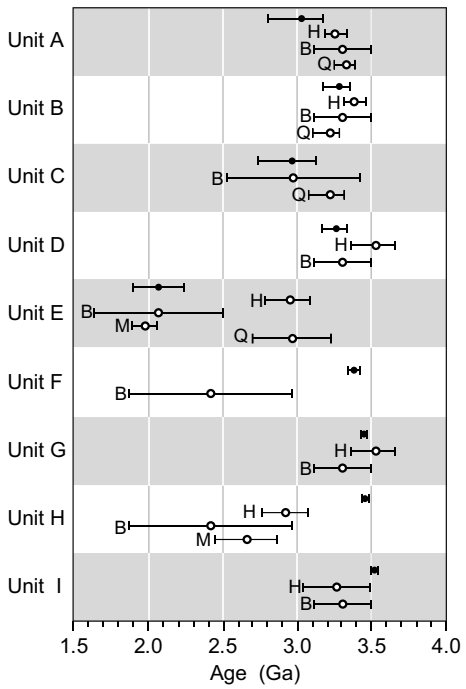

Fig. 4 The ages of the mare units in the study area. *Solid circles* with *error bars* indicate the ages determined in this study. The *bars* depict the plus–minus standard deviations. *Open circles* indicate the ages determined in previous studies; H, Hiesinger et al. (2000); B (Bugiolacchi and Guest 2008); M (Morota et al. 2011); Q (Qiao et al. 2014). In cases where their divisions of the mare units are significantly different from ours, their ages are not shown in this diagram

inviscid (Basaltic Volcanism Study Project 1981) that they made level surfaces at the time of deposition, a mare unit that is dammed by a ridge is younger than the formation of the ridge, and a deformed one is older than the formation of the ridge. Bryan (1973) and Schaber (1973) applied this technique to ridges in southwestern Imbrium, where high-resolution images taken by the Apollo missions were available. In addition, the high-resolution TC and NAC images allowed us to determine the formation ages of the lobate scarps and grabens, by using the degradation levels of small craters (Moore et al. 1980).

There are 'islands' including Montes Recti along the second inner ring in northern Imbrium (Spudis et al. 1988). We used the informal names of the islands, Chajorra and Alta Vista, which were introduced by Lee (1864), for convenience (Fig. 2a).

Mare ridges

The mare ridges in our study area have been already mapped by Schaber (1969) and M'Goniǵle and Schleicher (1972). We used the labels, Ridge Systems A through F, to refer to major mare ridges in the study area (Fig. 2). Among them, Ridge Systems A, B and C are part of the concentric systems of the most prominent ring structure of the Imbrium basin (Spudis 1993).

Ridge System A

Ridge System A consists of two arches and several narrow and short ridges with ENE-WSW trends from the south of Promontorium Laplace to the mountain Alta Vista (Fig. 2d). The arches are about 170 km long, 30 km wide and 200 m high relative to the surrounding plain. The arch is surmounted by elongated hills that have maximum peak heights of ~400 m relative to the surrounding plain (Fig. 2b, d). The hills make a right-stepping en echelon array.

As Whitaker (1972) pointed out, Ridge System A dams a mare unit (Figs. 2, 5). He assigned the formation age of the ridges vaguely as sometime in the Eratosthenian Period. We determined the age more precisely. The ridges of this system are blanketed by Units A, B, C and D, whereas the boundary between Units C and E outlines the southwestern foot of Ridge System A (Fig. 5). Accordingly, Units A, B, C and D are deformed along Ridge System A, which dams Unit E. Ridge System A deformed Units A, B, C and D and dammed the lavas of Unit E. Therefore, the major formation of Ridge System A was sometime after 2.97 Ga and before 2.07 Ga. The older limit is defined by the age of Unit C—the youngest of the four deformed units.

A part of the lower slope of the arch is exceptionally blanketed by Unit E (Fig. 5). There is no fissure along the

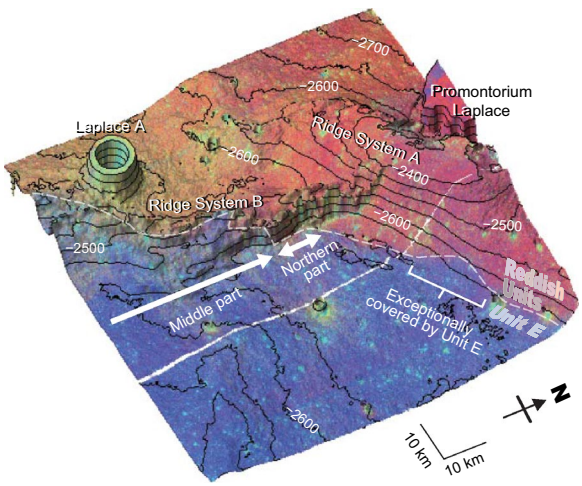

Fig. 5 Three-dimensional topographic models on which spectral ratio images are mapped. Intersecting area of Ridge Systems A and B. *Solid contour lines* indicate the altitude. The contour interval is 50 m. The vertical exaggeration is 50. The highland and the rim of Laplace A are truncated at −2300 m to enhance the mare ridges. Locations lacking in the MI data are indicated by the N–S trending white stripe. The *dashed line* indicates the northwestern border of Unit E

ridge that could feed the lavas of Unit E, suggesting that part of the ridge was reactivated and uplifted after the deposition of Unit E.

Ridge System B

Ridge System B consists of relatively narrow NNE-SSW trending ridges between the promontories Laplace and Heraclides. The ridges have heights and widths of 100–200 m and several kilometers, respectively. The southeastern segments of this group coincide with the rim of the Sinus Iridum basin, which was excavated at 3.7–3.84 Ga (Wagner et al. 2002). We subdivided the system into the northern, middle and southern parts at the latitudes of 45 and 42°N (Fig. 2b, c).

In the northern part, Units A and B are deformed by this system (Fig. 2d), which dams Unit E (Fig. 5). The fact that the surface of Unit E does not tilt but becomes thicker toward the ridge system (Section 3.2; Fig. 19) provides positive evidence that Unit E is dammed by the ridges. The northern part was formed after the deposition of Unit A and before the deposition of Unit E.

In the middle part, Ridge System B (Fig. 2c) deforms the unclassified unit around Laplace A and partly dammed Unit E (Fig. 5). The depositional age of the unclassified unit could not be determined because of heavy contamination by secondary craters. However, the spectral feature of the unit is similar to those of Units A and F. It might indicate that the depositional age of the unit is around 3.3 Ga. Unit E is partly deformed and partly dammed along the foot of the eastern edge of Ridge System B. Therefore, the middle part was tectonically active around the timing of the deposition of Unit E.

The southern part of Ridge System B is covered by Unit E, except for two small reddish islands around 41°N, 31° W (Fig. 2c). Accordingly, most of the southern part is younger than Unit E, but the islands began to be uplifted before the deposition of Unit E. The areas of the islands are too small so that their depositional ages were not determined.

Accordingly, the uplift of the northern part began after 3.25 Ga, which is the age of Unit A, and ceased before 2.07, which is the age of the dammed unit. The middle part of this system was mainly formed around 2.07 Ga, and the formation might begin after 3.25 Ga. The southern part of this ridge system is younger than 2.07 Ga.

Ridge System C

Ridge System C is the northern part of Dorsum Heim and consists of two N-S trending ridges, a prominent one and narrow one, to the southeast of Promontorium Heraclides (Figs. 1, 2b). The prominent ridge at 31.0° W is about 20 km wide and 200–400 m high, whereas the narrow one at 29.5°W has a height on the order of 10^1 m and a width of a few kilometers. North of 39°N and south of 37.5°N, Ridge System C is covered by Unit E, indicating the formation after 2.07 Ga. However, the middle part of this system around 38° N could be older, because the ridge system is not covered by Unit E but by an older spectrally reddish unit.

Ridge System D

The NNE–SSW trending narrow ridges in Sinus Iridum are called Ridge System D, in which three ridges are relatively prominent. They are about 100 m high, several kilometers wide and shorter than 100 km in length. Units F and I are involved in this ridge system, indicating that the ridges were formed sometime after 3.39 Ga.

Ridge System E

Ridge System E is composed of N–S trending ridges that make an array at 19° W, northeast of the Le Verrier (Fig. 2a, b). Each ridge is about 100 m high and 5 km wide. Ridge Systems A and E crosscut at 47.3°N, 19.0°W, but their order of formation is not clear. Units D, E and G are affected by this system. Accordingly, the ridge system was formed sometime after 2.07 Ga in Unit E, but those in Units D and G could be older.

Ridge System F

Ridge System F consists of N–S trending mare ridges in the northeastern part of the study area (Fig. 2b). The ridges of this system have heights and widths of ~150 m and several kilometers, respectively. This system meets Ridge System A and a NW-SE trending arch to the south of Mons Chajorra (Fig. 2b). Ridge System F involves Unit D. The depositional age of the unit places the maximum age of the formation at 3.27 Ga.

Ruptured craters along ridges

There are a number of ruptured craters along the mare ridges, which are recognized in the high-resolution images taken recently by SELENE TC and LRO-NAC. We interpreted that the craters are ruptured by thrust faults constituting mare ridges, because some of the ruptured craters are deformed and some of them are partly hidden by the hanging wall (Fig. 6). The ages of ruptured craters are the clues to the timing of tectonic deformations, because the craters must exist before the end of the tectonic activities. Figure 6a shows an example of the small ruptured craters. In the image, the thrust sheet covers half of the small crater. The sheet is slightly deformed probably for filling the depression of the crater. Examples of the small ruptured craters are also shown in Additional file 1: Figure S1. The kilometer-scale crater highlighted in Fig. 6b is an example of the largest ones. The crater is located in Ridge System E to the south of Montes

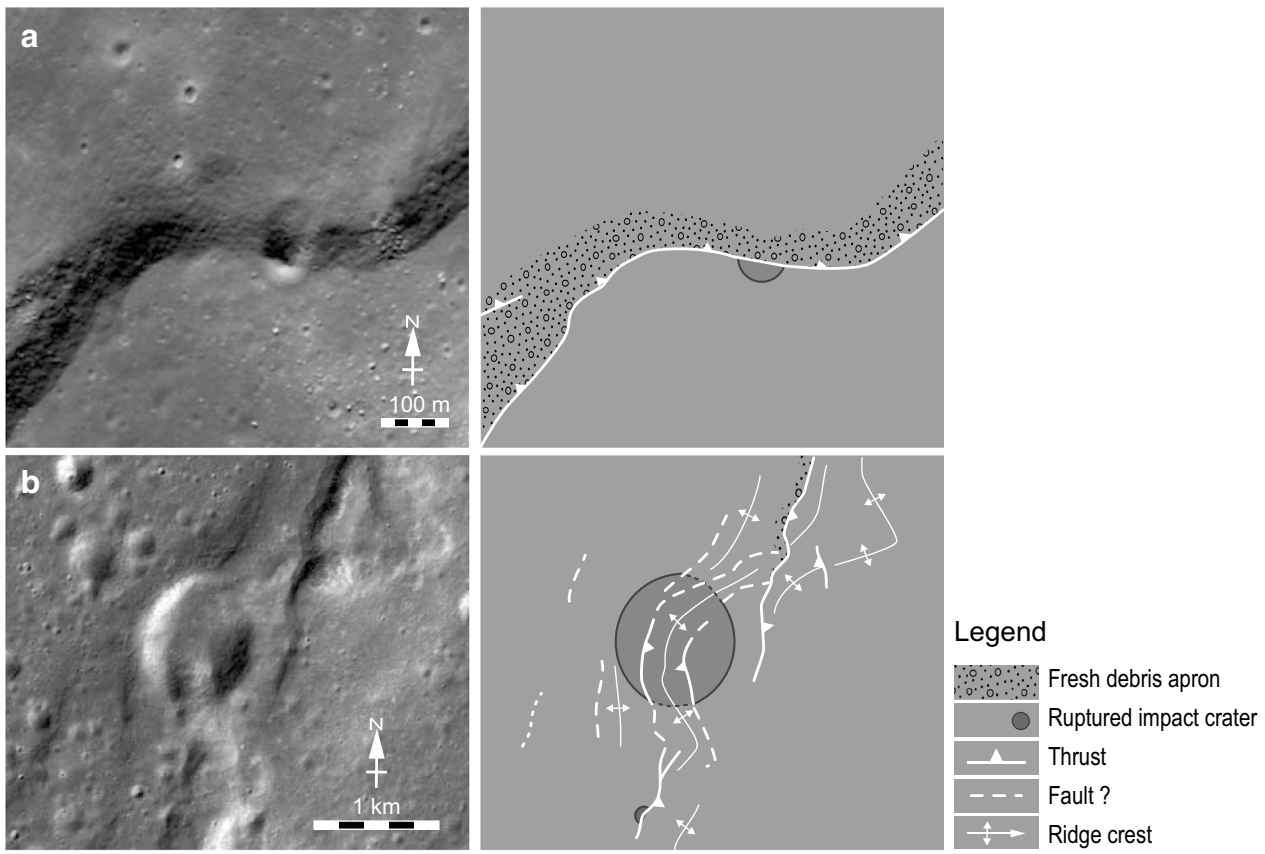

Fig. 6 Craters ruptured by thrust faults. **a** A small ruptured crater (48.14°N, 15.87°W) involved in Ridge System F (LROC NAC image M1149624430RC). The crater size is about 80 m in diameter. **b** Two craters ruptured by thrust faults involved in Ridge System E (LROC NAC image M1106037670LE). The larger one is located at the south of Montes Recti (47.7°N, 18.8°W)

Recti. It is not circular but elliptical in shape. The crater is shortened by two thrust faults along the N–S to NNE–SSW trending ridges. The crater floor is popped up by the faults. To the south of this crater, a crater with a diameter of 150 m lacks an eastern rim, which was destroyed by the over-thrusting or obliterated by talus deposits from the scarp along a ridge.

The ruptured craters are along all the ridge systems in the study area (Fig. 7). Some are as small as ~100 m in diameter, suggesting that the tectonic activities along ridges are geologically very young. On the basis of the degradation levels classified by Moore et al. (1980), the craters as small 100 m in diameter with shallow bowl-shaped morphology are classified as Copernican craters. The craters that are 80–100 m in diameter with gentle depression morphology are classified into the latest stage of Eratosthenian. In our analysis, the observed craters smaller than 100 m were categorized into shallow bowl-shaped craters, which suggest their formation ages are Copernican Period. Accordingly, all the ridge systems were at least partly active still in the Copernican Period. Note that the observed craters may contain secondary craters. Since it is a qualitative analysis, some of them might be formed in the Eratosthenian Period.

It is important to note that there are differences in the linear number densities of large ruptured craters (larger than 100 m in diameter; white circles in Fig. 7). Ridge System B, C and E deformed fewer large craters in Unit E than in the other units. In contrast, there is no difference in the linear number densities of small ruptured craters (smaller than 100 m in diameter; yellow circles in Fig. 7). This difference can be explained by the difference in the area density of craters depending on the depositional ages of the units.

Lobate scarps

There are lobate scarps in the study area (Fig. 2a). Among them, we detail the lobate scarps on the eastern and the western slopes of Montes Recti and Chajorra, respectively (Figs. 8a, 10a), because they affect the small Copernican craters. Both scarps have morphologically crisp terraces.

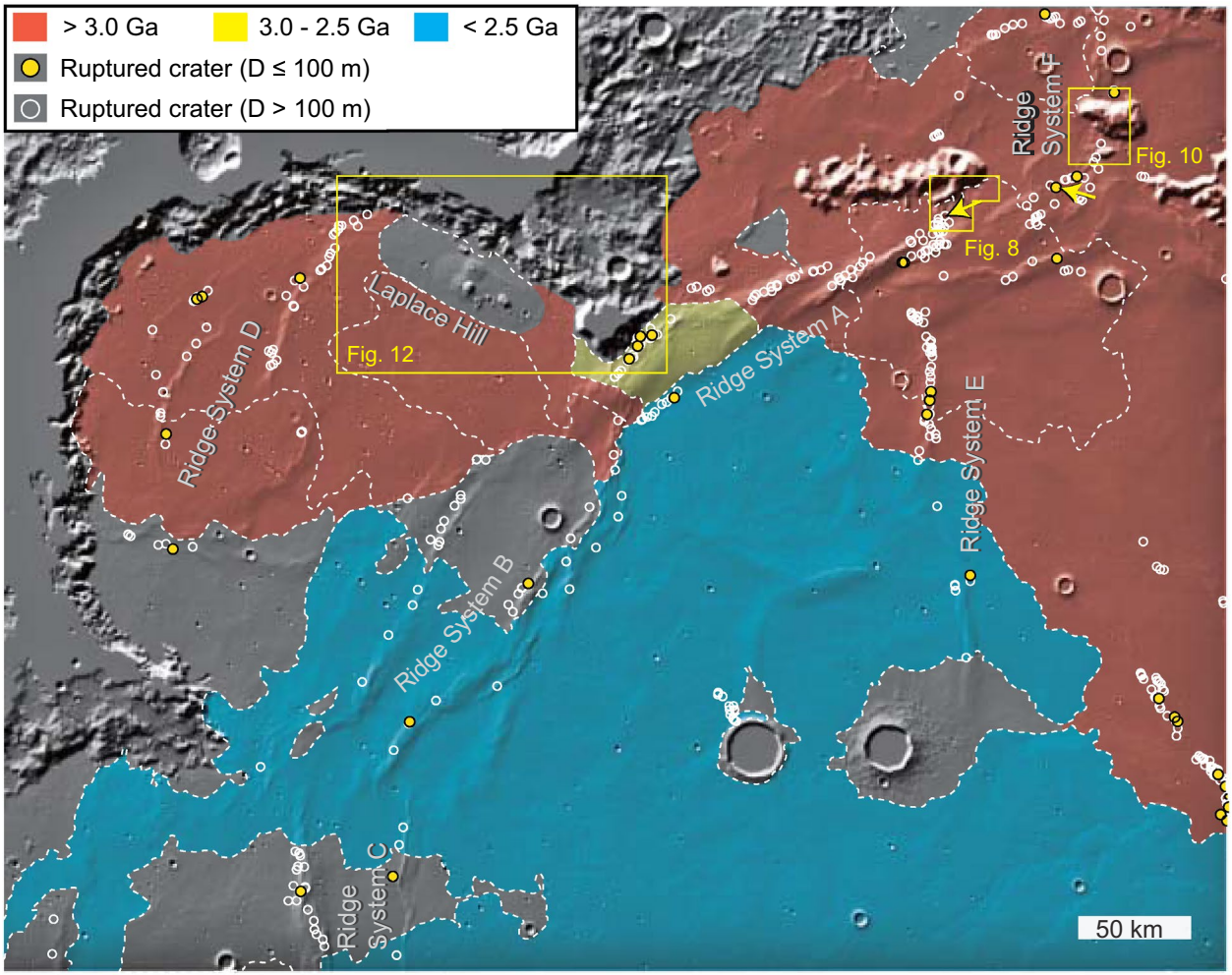

Fig. 7 Locations of ruptured craters are shown as circles. The ruptured craters larger and smaller than 100 m are shown in *white* and *yellow circles*, respectively. *Yellow arrows* indicate the locations of the ruptured craters shown in Fig. 6

Many terraces can be seen along the mare-highland boundaries on the Moon. They are thought of as the surface expressions of low-angle thrust faults (e.g., Binder and Gunga 1985; Watters et al. 2010; Williams et al. 2013), although they were interpreted as depositional features by some previous studies (Holcomb 1971; Greeley and Spudis 1978; Young 1976). We prefer the tectonic interpretation, because the lobate scarps along the slopes of Recti and Chajorra transform into mare ridges (Figs. 8, 10). Their crisp morphology suggests that they are formed in the Copernican Period (Watters et al. 2012). Some lobate scarps are thought to be even younger than 50 Ma from the crosscut relationships between the scarps and small ruptured craters, whose formation ages were estimated to be younger than 50 Ma (Watters et al. 2015).

Montes Recti

A branch of Ridge System E turns into lobate scarps at the mare-highland boundary of Montes Recti (47.95°N, 18.36°W; Fig. 8a, b). A lobate scarp runs along the southern margin of Montes Recti to make crisp terraces at the height of ~100 m from the neighboring plain (Fig. 8a). The terraces are tens of meters in width. The lithology of the slope between the terraces and the mare-highland boundary is not clear in their spectral features. However, we interpreted that the terraces are debris aprons, because there are craters with mountainside parts obliterated at the mare-highland boundary (Fig. 8b). There are grooves along the mountainside edges of the terraces (Fig. 8b).

The following observations indicate that the origin of the terraces is compressional tectonics. The southern

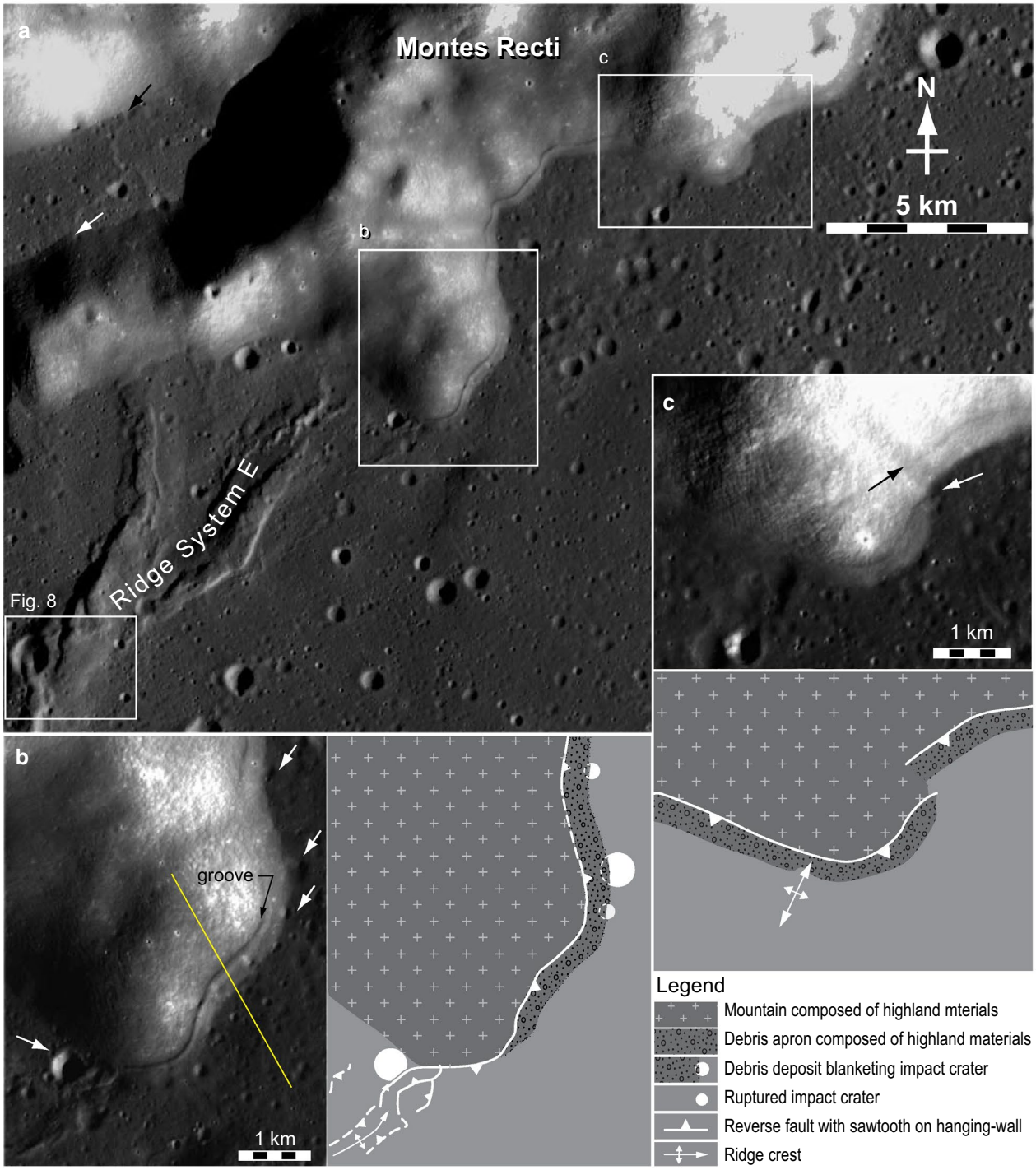

Fig. 8 Images of the eastern part of Montes Recti. **a** SELENE TC image of the region. *Arrows* indicate minor lobate scarps. There are prominent lobate scarps along the southeastern margin of this mountain, the close-ups of which are shown in the subfigures. **b** A groove and overlain craters by debris are shown (LROC NAC image M1136661568LC). The topographic profile along the yellow line is shown in Fig. 9. **c** A stepover (LROC NAC image M190724156RC). See text for details

segment is an extension of a ridge belonging to Ridge System E (Fig. 8b), and the terraces have a stepover structure (Fig. 8c). The section across the lobate scarp is shown in Fig. 9. The connection of the segment and Ridge System E suggests that the terraces were not formed by normal faulting, but thrusting. The slope dip of the mountain is

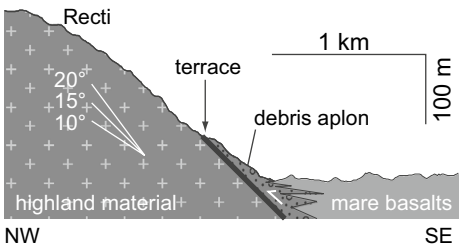

Fig. 9 Topographic profiles and the cross section for the subsurface structures at the southeastern Montes Recti. See Fig. 8b for the lines of the topographic profiles

about 15°. There is no critical evidence that shows the thrust plane parallel to the slope of Montes Recti, but we consider that the thrust surface runs along the slope of Montes Recti because of the following reasons. First, the terraces meander along the margin of the mountain. A greater dip in the fault surface requires a greater curvature of the fault surface. Second, it is natural that a weakness plane, such as a lithological boundary, is used as a fault plane.

A ruptured crater on a ridge in Fig. 8b has a clear rim. Its degradation level indicates a late Eratosthenian to mid-Copernican age (Moore et al. 1980). Accordingly, the thrusts involving the lobate scarps and the mare ridge just at the south of Recti were active in the Copernican Period. This young activity is consistent with the morphologically crisp and undegraded appearance of the terraces.

Mons Chajorra

There are lobate scarps at the western margin of Mons Chajorra and an 'isle' to the south of Chajorra (Fig. 10a). The scarps have crisp terraces at the heights of ~150 m (Fig. 10b) from the neighboring mare surface. There are grooves at the mountainsides of the scarps on the southwestern flank of Chajorra and on the western flank of the isle, indicating that the terraces are not made of debris from the mountain top. We interpreted that the terraces are surface expressions of westward-dipping thrusts, because the slope on the mare side of the scarp on Chajorra seems to underlie the mare basalt that slid up along the fault with the fault surface subparallel to the slope. The spectral feature of the strip between the terrace and the mare-highland boundary is basically as reddish as that of the neighboring mare and is contaminated by bluish spots probably due to the highland materials derived from the top of Chajorra (Fig. 10c). This interpretation is supported also by the iron content map in Fig. 10d produced by the algorithm of Otake et al. (2012). The FeO content abruptly changes at the terraces. The slopes lower than the terraces are poor in FeO (Fig. 10d). It indicates that the slopes lower than the terraces are composed of mare materials and are powdered by highland materials.

In addition, the following observations also indicate that the scarps are the surface expression of thrust faults. First, they turn into a mare ridge comprising Ridge System F. Second, the scarp bifurcates on the southwestern flank of Chajorra (Fig. 10b). Third, the mare surface steps down across the ridge connected with the scarps from west to east between Chajorra and the southern isle (Fig. 10e). Fourth, the upper branch of the bifurcated scarp in Fig. 10b has a crenulated trace on the slope with a wavelength and amplitude of 100 and 50 m, respectively (Fig. 10f), possibly the surface manifestation of a hinterland-dipping duplex (Twiss and Moores 2006, p. 125).

If the thickness of the thrust sheet is constant, the geological cross section inferred from the above-mentioned observations is shown as Fig. 11. The slope is inclined at ~ 25° around the terrace, which is approximately equal with the dip of the fault. The thrust sheet composed of the mare basalts has, therefore, a thickness of ~30 m which is the width of the terraces. We interpreted that a thin-skinned-type deformation has occurred in this area. The thin strata made of the mare basalts was peeled off from its substrata and crept up along the slope. The mare should have had a level surface before the faulting. If the mons did not rise after the deposition of Unit D, the displacement of the thrust sheet can be calculated by the distance between the tip of the thrust sheet and the horizontal surface of the mare unit. The vertical displacement is about 200 m, and the displacement along the thrust fault is about 1.4 km (Fig. 11). The mare affected by the fault belongs to Unit D, which is about 3.27 billion years old. Accordingly, the thrust sheet crept up on the flanks of the mountains in the last 3 billion years. The morphologically crisp terraces suggest a geologically recent activity of the thrust system.

Grabens

Grabens around Promontorium Laplace

Schaber (1969) and Hurwitz et al. (2013) interpreted a sinuous rille around Promontorium Laplace (Fig. 2b) as a volcanic sinuous rille. It is obscure whether the rille was initially formed as a tectonic or a volcanic rille, but we interpreted that the rille is a tectonic graben from the following lines of evidence (Figs. 12, 13). To the west of the cape, two craters with diameters of ~140 and 250 m are dislocated along the rille (Fig. 13). The sinuosity can be explained because the preexisting zones of weakness of mare-highland lithological boundary were used as a fault plane.

The graben is ~30 km long and ~500 m wide with a depth of a few tens of meters. The northwestern end of the graben is buried by a debris apron at the foot of

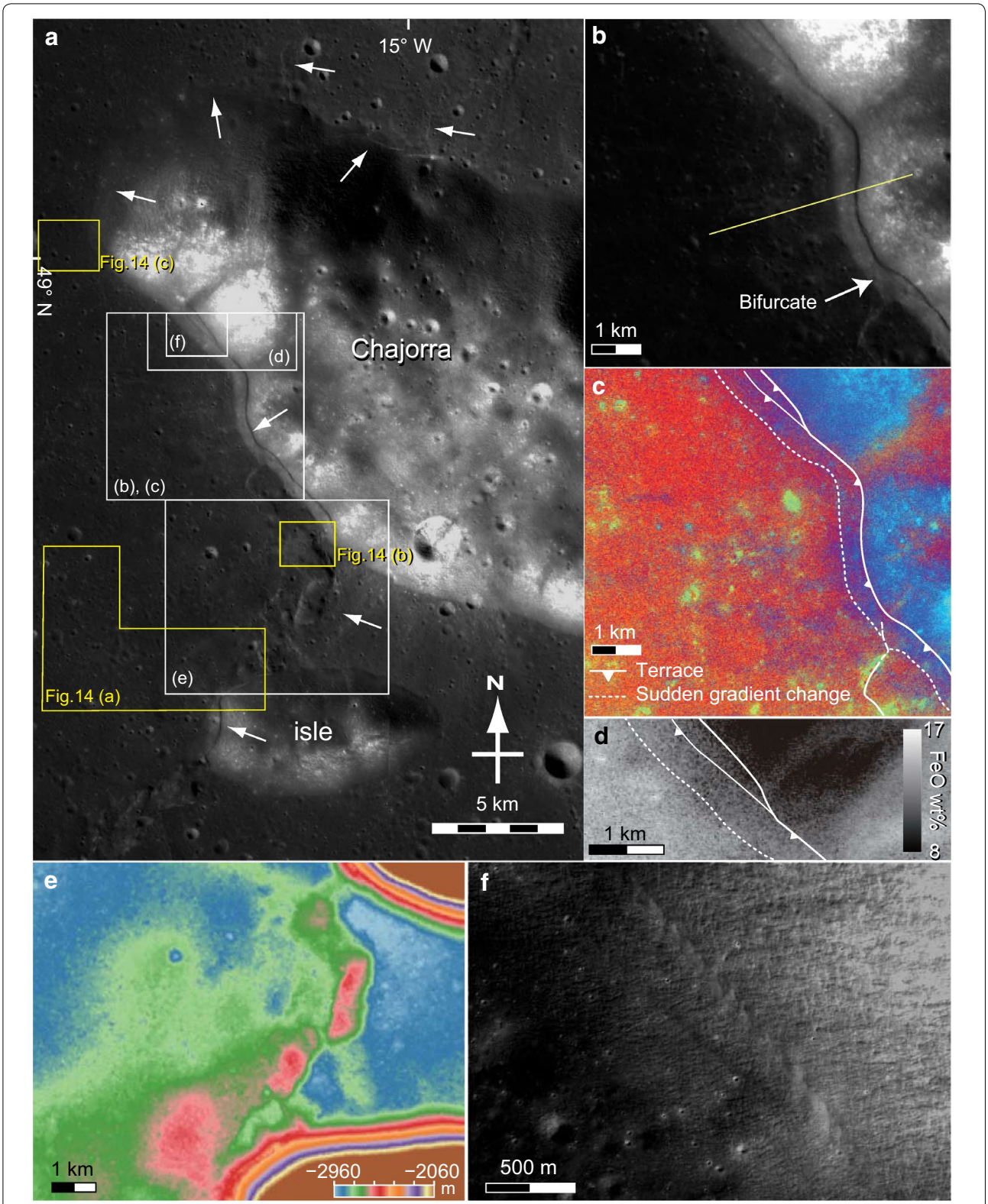

Fig. 10 Images of the western part of Mon Chajorra. **a** SELENE TC image of the region. Lobate scarps (*white arrows*) affect the western margins of Chajorra and the hill to the east of the mountain. The scarps are the continuations of Ridge F. *Yellow boxes* indicate the locations of the small fissures shown in Fig. 14. **b** The close-up of the scarps. Figure 11 shows the topographic profile along the *yellow line*. **c** MI image of the same area. **d** The iron content map. The iron content abruptly changes at the terrace. **e** Topography shows that the west area of the ridge is raised. **f** Crenulated structures at the terrace (LROC NAC image M1136640204RC)

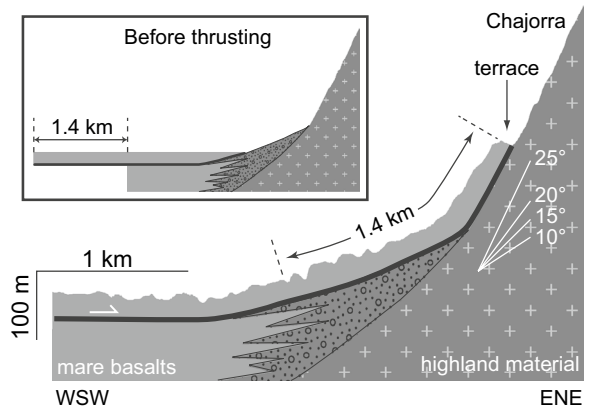

Fig. 11 Topographic profiles and the cross section for the subsurface structures at the western Mons Chajorra. The *inset* represents the inferred structure before thrusting. See Fig. 8 for the lines of the topographic profiles

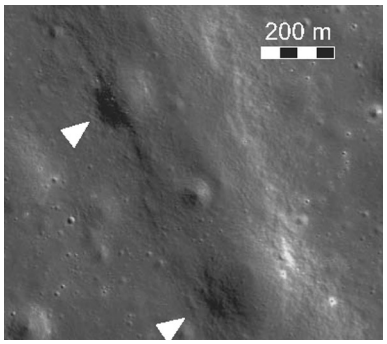

Fig. 13 Close-up of the rille to the west of the Promontorium. The southwestern cliff of the rille cuts two impact craters (*arrows*) with the radii of ~140 and 250 m (LROC NAC image M104690472LC)

Montes Jura (Fig. 12). The valley is formed on Unit C, which is 2.97 Ga. Therefore, the graben was formed after 2.97 Ga. In addition, based on the correlation of degradation levels and ages by Moore et al. (1980), the ages of the 140-m-diameter crater (Fig. 13) are classified into the early Copernican Period to late Eratosthenian Period. The larger one is classified into the Eratosthenian Period. Accordingly, the graben was tectonically active in the late Eratosthenian Period.

There are a few rilles along the mare-highland boundary between 26.5 and 28.1°W, roughly on the extension of the graben (Fig. 12). It is difficult to distinguish whether they are volcanic or tectonic in origin. Their sinuosity suggests a volcanic origin (Hurwitz et al. 2013), but the location just along the boundary suggests a tectonic origin using the lithological boundary.

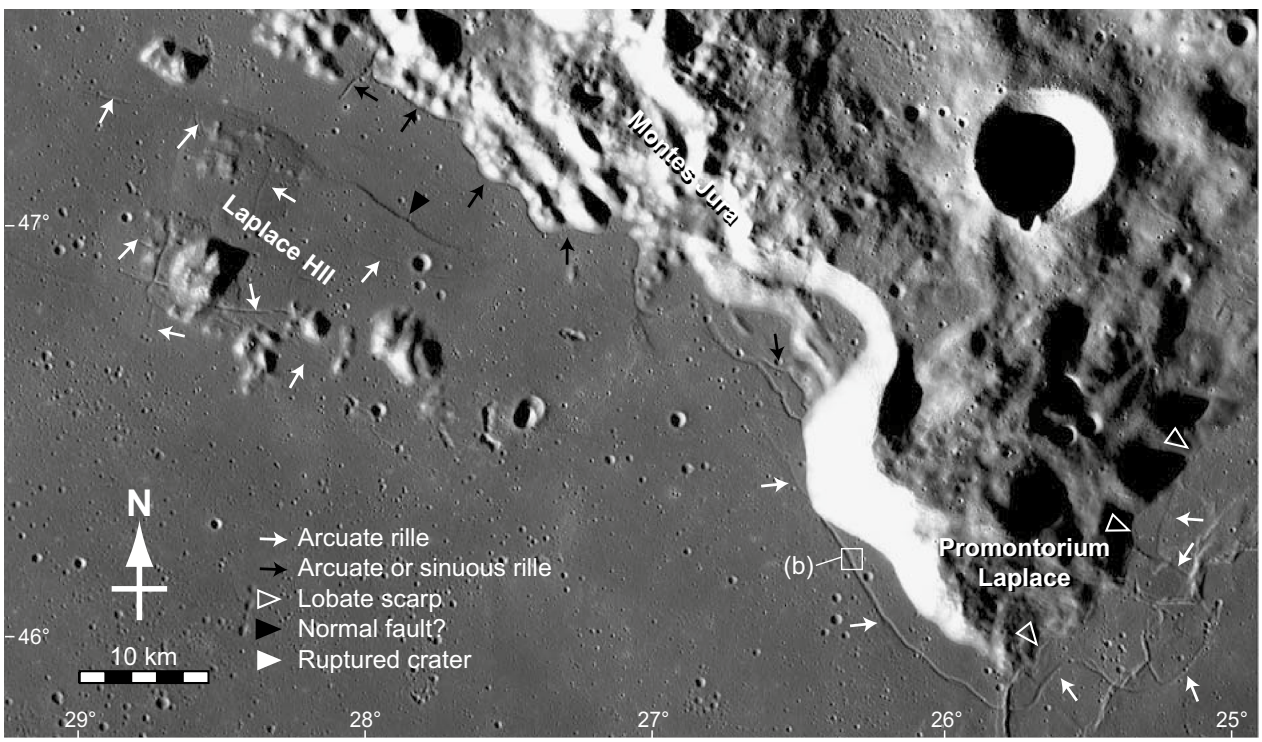

Fig. 12 Images of the rilles around Promontorium Laplace. SELENE TC image of the region. *Arrows* point to arcuate rilles, the local trends of which are perpendicular to the *arrows*

Grabens around Mons Chajorra

There are small-scale grabens or fissures on the western side of the lobate scarps around Mons Chajorra (Fig. 14). We named the grabens, Graben Systems A, B and C from south (Fig. 14a–c). French et al. (2015) interpreted the small-scale grabens near the lobate scarps and mare ridges as secondary structures associated with the formation of such map-scale contractional structures. We also interpreted Graben Systems A, B and C as grabens associated with the formations of the lobate scarps.

Graben System A has a total length of 7–8 km and consists of more or less straight fissures each of which are 10^1 and 10^2 m in width and length, respectively. The fissures are terminated at the sharp bend of the lobate scarp

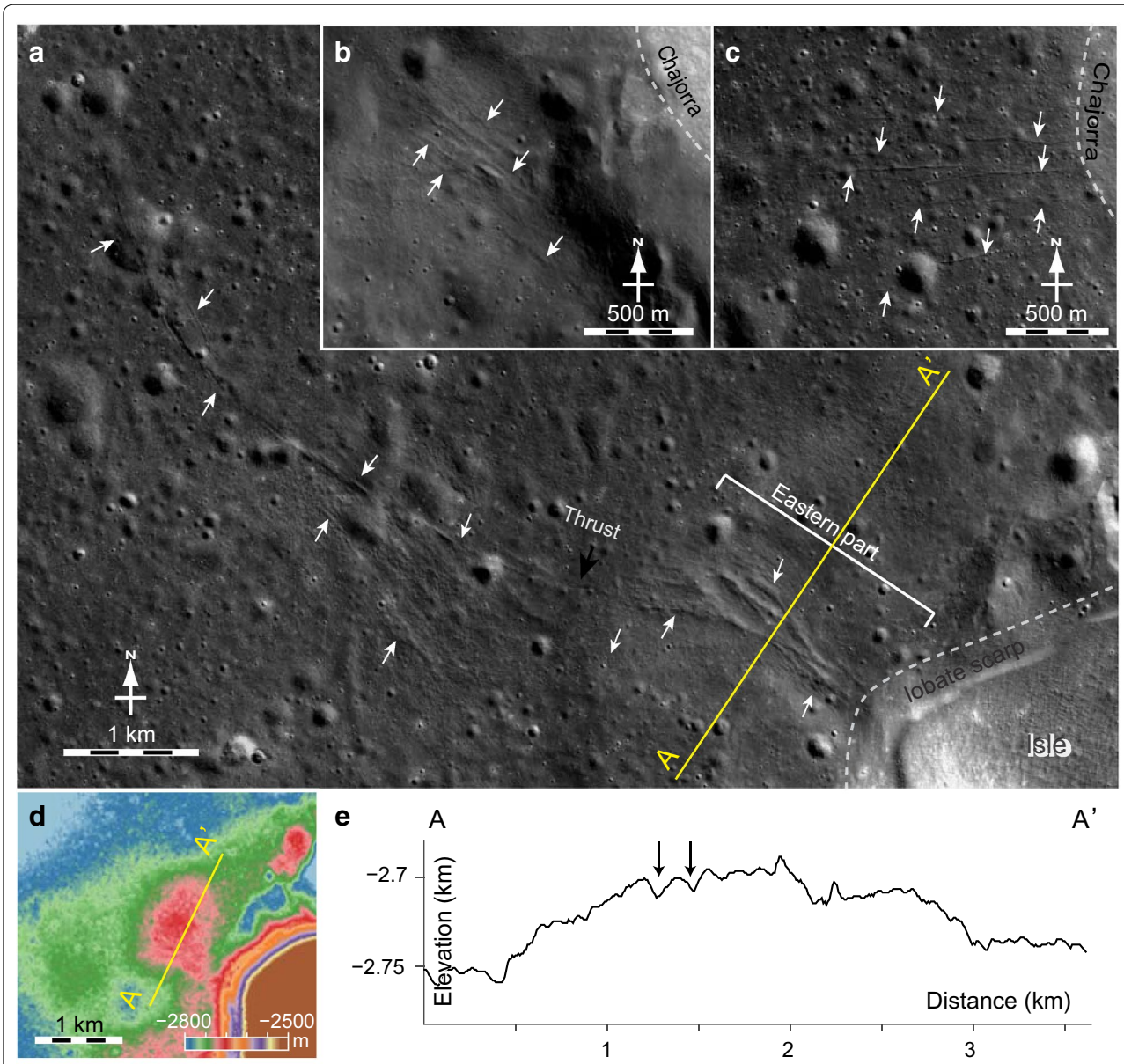

Fig. 14 Small-scale grabens (*arrows*) around Mons Chajorra. Their locations are shown in Fig. 10. *Dashed lines* indicate the foot lines of the mountain and the isle. **a** Graben System A (48.50°N, 15.42°W) at the south of Mons Chajorra and the west of an isolated island (LROC NAC images M1098943917LC and M129573848LC). **b** Graben System B (48.66°N, 15.17°W) at the south of Mons Chajorra (LROC NAC image M1129573848RC). **c** Graben System C (49.01°N, 15.62°W) at the northwestern tip of Mons Chajorra (LROC NAC image M10983917LC). **d** Kaguya DTM image around Graben System A. **e** The cross section along the *yellow line* shown in (**d**). Topographic profile of a small bulge and two grabens (Kaguya DTM). Vertical exaggeration is 10. *Arrows* indicate the locations of fissures

on the western foot of the isle to the south of Chajorra. The system has a convex-southwestward curvature and splays at its western end. In this western part, fissures make a left-stepping en echelon arrays, suggesting a dextral strike-slip component. The system includes a short segment of thrust fault (Fig. 14a). Strike-slip tectonic structures sometime involve extensional and compressional tectonic features. However, no crater is dislocated with this sense of shear, indicating very small strike-slip movements, if any. Grabens at the eastern part of Graben System A are the widest and deepest among the grabens around Mons Chajorra. The width and the depth are ~150 and 10 m, respectively (Fig. 14d, e). The eastern part is on a small bulge (Fig. 14d, e). Accordingly, we interpreted that the grabens were formed as an incipient oblique transfer fault to accommodate the differential eastward sliding of the thrust sheet on the north and south side of the sharp bend.

Graben System B consists of fissures that are 10^1 and 10^2 m order in width and length, respectively. They are generally straight, parallel to each other and lie along the crest of the mare ridge that turns into the lobate scarps on Mons Chajorra (Fig. 14b), suggesting that they were formed by flexural bending of the thrust sheet.

Graben C System consists of E–W trending straight fissures extending from the western tip of the Mons Chajorra. Their widths and lengths are about 10^1 and 10^2 m in width and length, respectively.

Graben Systems A and C dislocated craters smaller than 100 m in diameter, indicating their formation ages of the Copernican Period (Fig. 15). These young graben formations present with lobate scarps support that the scarps are young tectonic deformations. French et al. (2015) analyzed small grabens and concluded that the small grabens are no older than late Eratosthenian from the crosscutting relationships of small craters to grabens. The result corresponds to our result.

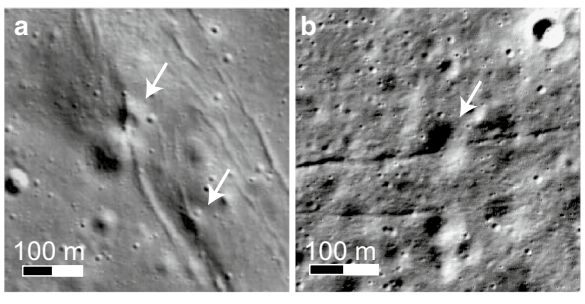

Fig. 15 Small craters ruptured by grabens around Mons Chajorra. **a** ~60- and 50-m crater dislocated by Graben A (LROC NAC image M1098943917LC). **b** ~70-m crater dislocated by Graben C (LROC NAC image M1121352379RC)

Grabens on Laplace Hill

There are straight rilles on a bulge at the northwestern foot of Ridge System A. We refer to the bulge as Laplace Hill in this study (Fig. 2d). The hill has an oval planar shape extent. The lengths of its major and minor axes are 40 and 30 km, respectively. Laplace Hill has a height of ~ 150 m relative to the surrounding plain (Fig. 16) and is surmounted by several peaks of about 50–500 m above the bulge. The bulge is covered by mare basalt, which is evidenced by its spectral features (Fig. 2c). The spectral feature of the unit is slightly different from the neighboring Unit B (Fig. 2). The peaks have rugged surfaces with the spectral features similar to those of Montes Jura, except for the peaks at −2570 m with a spectral feature similar to the surrounding mare basalt. The straight rilles on the hill have depths and lengths of ~30 m and < 20 km, respectively (Fig. 12). We interpreted them as grabens, because they are straight and cut the peaks on the hill (Fig. 16).

According to the morphology, the dome is originated from volcanic activity. Lena et al. (2013) named the northwestern part of the hill as the dome 'L6' (Fig. 16). They named the lumpy top of the hill around the peaks at −2030 and −2570 m as 'L5.' Both domes were interpreted from their topography to be lava domes.

The formation ages of the grabens are not evident, because the age of the deformed unit on the hill was not determined. However, the fact that there is no graben extending into Unit A suggests that they are probably older than Unit A, which adjoins and is younger than the

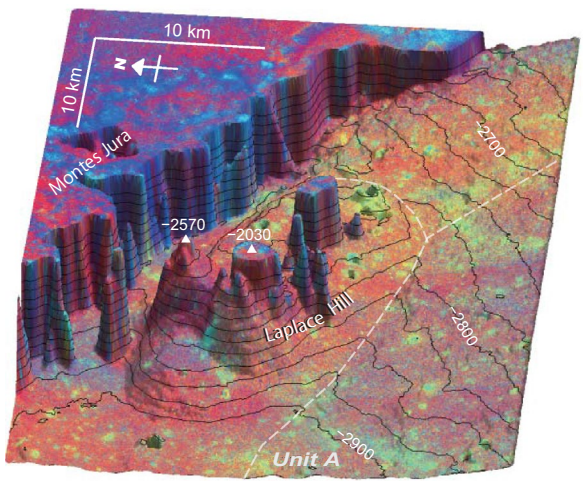

Fig. 16 Three-dimensional topographic models on which spectral ratio images are mapped. Topography around Laplace Hill. Montes Jura and peaks on the hill are truncated at −2600 m. Vertical exaggeration is 25. Contour interval is 25 m. Unit boundary is shown by a *dashed line*, a part of which lies along the southern foot of the hill. *Triangle* indicates a peak at the altitude of −2570 m

hill. The domal uplift of the hill might result in the graben formation atop the hill (Wöhler et al. 2009).

Discussion

The constraints on the ages of tectonic features have been described in the previous sections and are shown in the map of the study area in Fig. 17. Some ridges in the study area initiated their deformation after 2.07 Ga, indicated by the deformed Unit E (2.07 Ga). In addition, mare ridges, lobate scarps and thrust faults in the study area have been revealed to be active in the Copernican Period at many locations as evidenced by the distribution of the small ruptured craters (Fig. 19). The fissures nearby lobate scarps and mare ridges (Fig. 14) suggest young tectonic contraction as well. We also found a graben that was active after the late Eratosthenian Period near Promontorium Laplace. This has implications for their origins.

The mascon tectonic hypothesis becomes improbable in the study area. The mare ridges and grabens in and around the mascon basins are thought to result from the subsidence of super-isostatic loading of the mare basalts (Baldwin 1968; Wilhelms and McCauley 1971; Maxwell et al. 1975; Brennan 1976; Melosh 1978; Solomon and Head 1980), but the young tectonic deformations are inconsistent with the hypothesis. The loading should have resulted in more or less syndepositional tectonics (Solomon and Head 1979, 1980). Most of mare units in Imbrium basin are older than ~3.0 Ga (Hiesinger et al. 2000; Bugiolacchi and Guest 2008; Morota et al. 2011), suggesting the weight of the mare basalts had been built up mostly until ~3.0 Ga.

The loading of the youngest mare unit (Unit E; 20.7 Ga) is the one that could induce mascon tectonics, but the following evidence indicates that the weight of Unit E is

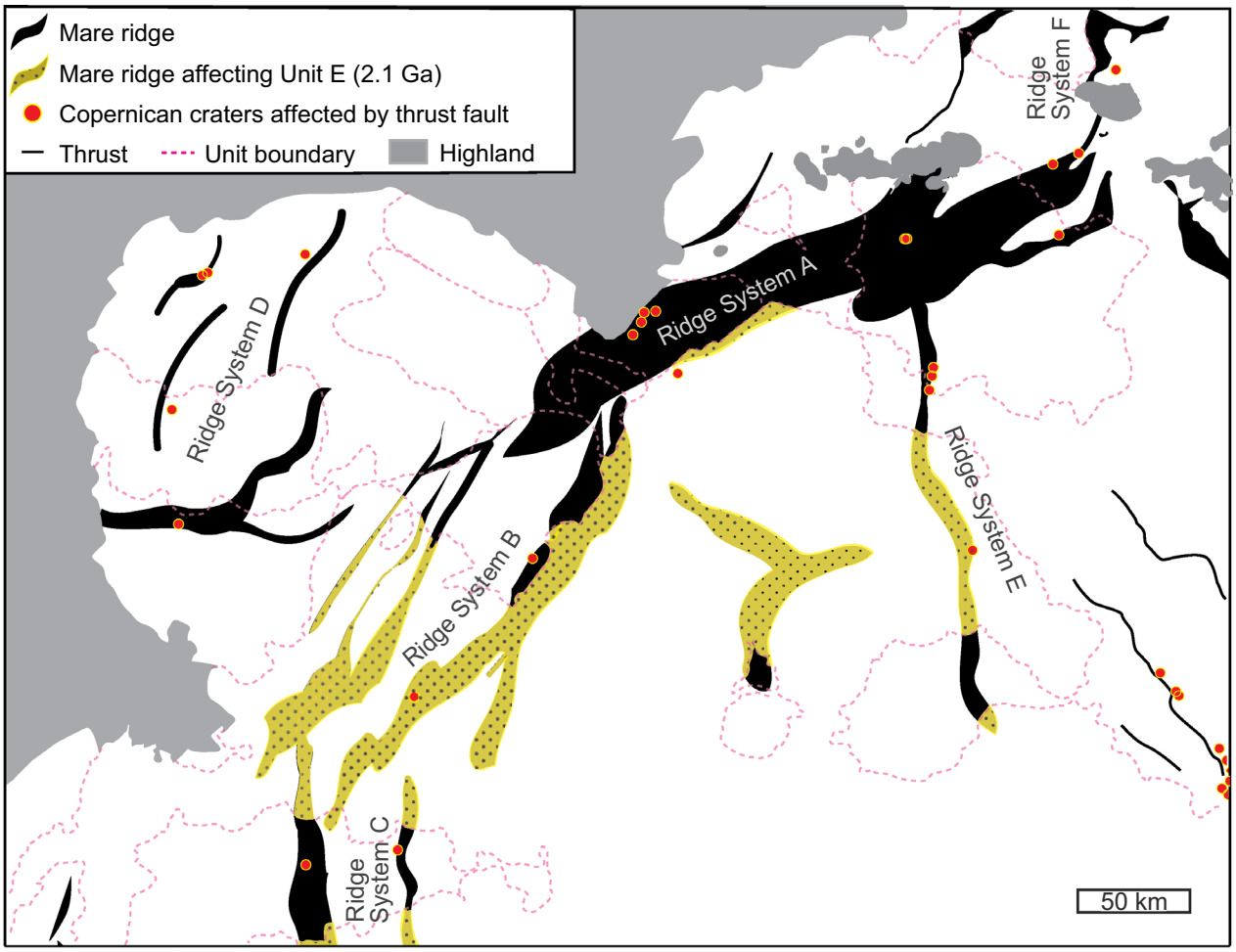

Fig. 17 The formation history of the mare ridges is shown. The *yellow regions* indicate the regions that were tectonically active after 2.1 Ga. The *reddish points* indicate the tectonically active areas in the Copernican Period. Our study area is tectonically active all over the region

insufficient to induce mascon tectonics. The sharp spectral contrast between bluish Unit E and the other reddish older units (Fig. 2c) allows us to infer the thickness of the unit by using the small craters that penetrate through Unit E. The depth of a simple crater is about 1 / 5 of its diameter (e.g., Pike 1977). For example, if a 500-m-diameter crater penetrates through the uppermost unit and reaches to the underlying unit, the thickness of the uppermost unit at the point is estimated to be thinner than ~100 m. We used spectral ratio images to measure the diameters of the craters penetrating the bluish unit and ejecting underlying reddish materials. A number of penetrating craters can be seen as reddish spots in Unit E in the spectral ratio image in (Figs. 2c, 18). Figure 19 shows the distribution and the sizes of such craters. Penetrating craters with diameters smaller than 500 m are distributed all over the study area. Accordingly, the general thickness of Unit E is less than a hundred meters. The small penetrating craters are sparse near Ridge System A and the north part of Ridge System B, indicating that Unit E becomes thicker toward the ridge systems. Since the mascon hypothesis assumes mare basalts as thick as several kilometers (e.g., Solomon and Head 1980), we regarded that the loading by Unit E is too small to yield deformations. Therefore, the tectonic activities by the mascon loading should have ceased around 3.0 Ga.

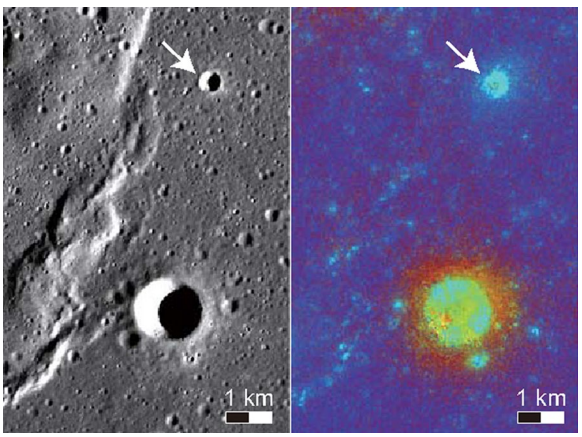

Fig. 18 One of the penetrating craters through bluish Unit E and ejecting underlying reddish lavas. (*left*) TC morning image. (*right*) Spectral ratio image. A crater (the largest crater; 41.02°N, 27.60°W) ejected underlying spectrally reddish lavas. There is a 400-m crater (*white arrow*) that penetrated into Unit E and did not penetrate through it

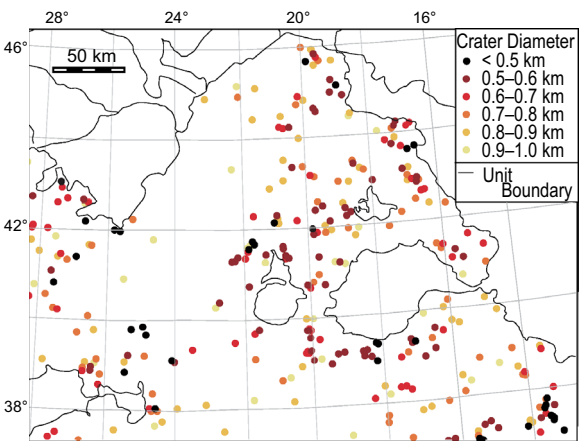

Fig. 19 Distribution of craters that penetrated through Unit E and reached to the underlying spectrally reddish mare unit

Ridge Systems A, B and C were thought to correspond to the inner most rings of the Imbrium basin (Spudis 1993). We revealed that the ridge systems were not originally formed to be the inner ring structure, because their formation ages are too young. The formations of the ridge systems were explained by the reactivation of basement faults that originated in the modification stage of a multiringed basin. Such a concentric fault was found in the Chicxulub impact crater (Morgan et al. 1997; Melosh 1997).

The origin of the forces driving young tectonism is attributed to the global cooling of the Moon and basin formation events. Radar sounding from SELENE revealed that major mare ridges in southern Serenitatis were significantly younger than the mare basalts in the region (Ono et al. 2009). High-resolution images taken by LROC showed lobate scarps as young as Copernican in age (Watters et al. 2010).

Geologically young extensional features have been reported by several researchers in some areas on the Moon, but the occurrence is different from the graben that we found near Promontorium Laplace (Fig. 13). Howard and Muehlberger (1973) found fissures along the crest of a mare ridge in Serenitatis. Watters et al. (2012) and French et al. (2015) found the swarms of fissures and grabens in the areas where the surface layers have been subjected to buckling along the crests of ridge-like rises. French et al. (2015) also reported globally distributed small-scale grabens that are not associated with compressional features. Regional uplift around the Promontorium may have resulted in the graben formation, but there is no direct evidence for this hypothesis. It is not clear whether the full width of the graben was entirely formed after the late Eratosthenian Period. Since the graben that we found is ~500 m wide and ~30 km long, the graben is morphologically different from those found by previous researchers. The grabens along positive topographic features swarm, and individual ones are ~40 m wide and ~500 m long (Watters et al. 2012; French et al. 2015). The grabens that are not associated with positive topographic features have a mean width and length of 19 and 146 m, respectively (French et al. 2015).

In addition to the global cooling, the young tectonism is explained by the regional thermal history of the PKT and the collapse of tidal bulges. The prolonged cooling is consistent with the fact that the area belongs to PKT where a relatively high thermal gradient has been kept by concentrated heat-producing elements in the lithosphere (Laneuville et al. 2013; Andrews-Hanna et al. 2014; Siegler and Smrekar 2014). The formation of the young graben near Promontorium Laplace may have been allowed by the relative uplift of the region by the thermal subsidence of the surrounding regions. The hot interior of the terrain may have mitigated the horizontal compression by the global cooling, as was suggested for the fresh grabens by Watters et al. (2012).

The collapse of tidal bulges of the Moon associated with the increase of the Earth–Moon distance should have resulted in a characteristic deformation pattern depending on latitudes and longitudes in the lunar lithosphere. The orbital evolution of the Moon had been constrained mainly from Phanerozoic strata and fossils on the Earth (e.g., Lambeck 1980), but in older ages this is controversial (e.g., Williams 2000). Transpressional tectonics was predicted in this area by Melosh (1980), consistent with the right-step en echelon arrangement of the ridges in Ridge System A. The ridge system began to be formed in the early Eratosthenian Period. Therefore, the details of the lunar tectonic history may place constraints on the orbital evolution.

Conclusions

We found lobate scarps and also mare ridges and grabens that are significantly younger than the majority of the mare basalt fills. Copernican tectonic structures are dominant in our study area. The origins of those young structures cannot be explained by the mascon loading hypothesis, although the distribution pattern of the tectonic structures shows typical feature of mascon tectonics. The distributions can be explained by reactivations using preexisting zones of weakness originated from impact structures, such as the inner ring of the Imbrium basin.

Additional file

Additional file 1. Examples of small ruptured craters by thrusts. **a** There is a bulge on the floor of the crater at 38.87°N, 14°W (LROC NAC image M1129574084RC). Thrusts deformed craters at **b** 46.26°N, 24.95°W (LROC NAC image M1167318888LC), **c** 42.62°N, 18.81°W (LROC NAC image M190731211LC), **d** 38.60°N, 29.62°W (LROC NAC image M150715327LC), **e** 40.42°N, 15.27°W (LROC NAC image M114056610LC) and **f** 47.89°N, 15.65°W (LROC NAC image M1149624430RC).

Authors' contributions

YD has designed this study and performed the analysis. AY and KS participated in the design of the study and contributed to the interpretation and the writing. TM supported performing the CSFD measurements. JH, MO and TM are the principal investigators of LISM, Kaguya, and provided the data sets. All authors read and approved the final manuscript.

Author details

[1] Division of Earth and Planetary Science, Kyoto University, Kyoto, Japan. [2] Institute of Space and Astronautical Science, Japan Aerospace Exploration Agency, Sagamihara, Kanazawa, Japan. [3] Graduate School of Environmental Studies, Nagoya University, Nagoya, Aichi, Japan. [4] Center for Global Environmental Research, National Institute for Environmental Studies, Tsukuba, Japan.

Acknowledgements

We are grateful to Koji Matsumoto for providing us the gravity model by using data obtained by GRAIL. We are also grateful to Nathan R. Williams and Satoru Yamamoto for giving us constructive comments and suggestions. This work was financially supported by JSPS (22340151).

Competing interests

The authors declare that they have no competing interests.

Received: 25 December 2015 Accepted: 30 August 2016
Published online: 20 September 2016

References

Andrews-Hanna JC, Jonathan B, Head JW III, Howett CJA, Kiefer WS, Lucey PJ, McGovern PJ, Melosh HJ, Neumann GA, Phillips RJ, Schenk PM, Smith DE, Solomon SC, Zuber MT (2014) Structure and evolution of the lunar Procellarum region as revealed by GRAIL gravity data. Nature 514:68–71. doi:10.1038/nature13697

Baldwin RB (1968) Lunar mascons: another interpretation. Science 162:1407–1408. doi:10.1126/science.162.3860.1407

Basaltic Volcanism Study Project (1981) Basaltic volcanism on the terrestrial planets. Pergamon, New York

Binder AB, Gunga H-C (1985) Young thrust-fault scarps in the highlands: evidence for an initially totally molten Moon. Icarus 63:421–441

Brennan WJ (1976) Multiple ring structures and the problem of correlation between lunar basins. In: Proceedings of the 7th lunar science conference, pp 2833–2843

Bryan WB (1973) Wrinkle-ridges as deformed surface crust on ponded mare lava. In: Proceedings of the 4th lunar science conference, pp 93–106

Bugiolacchi R, Guest JE (2008) Compositional and temporal investigation of exposed lunar basalts in the Mare Imbrium region. Icarus 97:1–18. doi:10.1016/j.icarus.2008.04.001

Fischer EM, Pieters CM (1994) Remote determination of exposure degree and iron concentration of lunar soils using VIS-NIR spectroscopic methods. Icarus 111:475–488. doi:10.1006/icar.1994.1158

French RA, Bina CR, Robinson MS, Watters TR (2015) Small-scale lunar graben: distribution, dimensions, and formation processes. Icarus 252:95–106. doi:10.1016/j.icarus.2014.12.031

Gilbert GK (1893) The Moon's face, a study of the origin of its features. Philos Soc Wash Bull 12:241–292

Greeley R, Spudis PD (1978) Mare volcanism in the Herigonius region of the Moon. In: Proceedings of the 9th lunar and planetary science conference, pp 3333–3349

Haruyama J, Matsunaga T, Ohtake M, Morota T, Honda C, Yokota Y, Torii M, Ogawa Y (2008) LISM Working Group. Global lunar-surface mapping experiment using the lunar imager/spectrometer on SELENE. Earth Planet Space 60:243–255

Hiesinger H, Jaumann R, Neukum G, Head JW (2000) Ages of mare basalts on the lunar nearside. J Geophys Res 105:29239–29275

Holcomb R (1971) Terraced depressions in lunar maria. J Geophys Res 76:5703–5711

Howard KA, Muehlberger WR (1973) Lunar thrust faults in the Taurus-Littrow region. In: Apollo 17: preliminary science report, vol 330, pp 22–31

Hurwitz DM, Head JW, Hiesinger H (2013) Lunar sinuous rilles: distribution, characteristics, and implications for their origin. Planet Space Sci 79–80:1–38. doi:10.1016/j.pss.2012.10.019

Ivanov BA, Neukum G, Wagner R (2001) Size-frequency distributions of planetary impact craters and asteroids, in Collisional processes in the Solar System. edited by Marov, M.Y. and Rickman. Astrophys. Space Sci. Libr. 261:1–34

Kato M, Sasaki S, Takizawa Y (2010) The Kaguya mission overview. Space Sci Rev 154:3–19. doi:10.1007/s11214-010-9678-3

Lambeck K (1980) The Earth's variable rotation: geophysical causes and consequences. Cambridge University Press, New York

Laneuville MMA, Wieczorek D Breuer, Tosi N (2013) Asymmetric thermal evolution of the Moon. J Geophys Res Planets 118:1435–1452

Lee J (1864) On the Lunar "Mare Smythii," the walled Plain "Rosse," the "Percy Mountains," and the newly named Craters, "Phillips," "Wrottesley," "Chevallier," and "Piazzi Smyth." In: Rep. BAAS 1863 Meeting, pp 7–9

Lemonie FG, Goossens S, Sabaka TJ, Nicholas JB, Mazarico E, Rowlands DD, Loomis BD, Chinn DS, Caprette DS, Neumann GA, Smith DE, Zuber MT (2013) High-degree gravity models from GRAIL primary mission data. J Geophys Res Planets 118:1676–1698

Lena R, Wöhler C, Phillips C, Chiocchetta MT (2013) Lunar domes: properties and formation processes. Springer, Milan

Lucey PG, Taylor GJ, Malaret E (1995) Abundance and distribution of iron on the Moon. Science 268:1150–1153. doi:10.1126/science.268.5214.1150

Maxwell TA, El-Baz F, Ward SH (1975) Distribution, morphology, and origin of ridges and arches in Mare Serenitatis. Geol Soc Am Bull 86:1273–1278

Melosh HJ (1978) The tectonics of mascon loading. In: Proceedings of the 9th lunar and planetary science conference, pp 3513–3525

Melosh HJ (1980) Tectonic patterns on a tidally distorted planet. Icarus 43:334–337. doi:10.1016/0019-1035(80)90178-5

Melosh HJ (1997) Multi-ringed revelation. Nature 390:439–440. doi:10.1038/37218

M'Goniǵle JW, Schleicher D (1972) Geologic map of the Plato quadrangle of the Moon. Rep., U.S. Geological Survey, Tech

Moore HJ, Boyce JM, Hahn DA (1980) Small impact craters in the lunar regolith—their morphologies, relative ages, and rates of formation. Moon Planets 23:231–252

Morgan J, Warner M, the Chicxulub Working Group, Brittan J, Buffler R, Camargo A, Christeson G, Denton P, Hildebrand A, Hobbs R, Macintyre H, Mackenzie G, Maguire P, Marin L, Nakamura Y, Pilkington M, Sharpton V, Snyder D, Suarez G, Trejo A (1997) Size and morphology of the Chicxulub impact crater. Nature 390:472–476. 10.1038/37291

Morota T, Haruyama J, Ohtake M, Matsunaga T, Honda C, Yokoya Y, Kimura J, Ogawa Y, Hirata N, Demura H, Iwasaki A, Sugihara T, Saiki K, Nakamura R, Kobayashi S, Ishihara Y, Takeda H, Hiesinger H (2011) Timing and characteristics of the latest mare eruption on the Moon. Earth Planet Sci Lett 302:255–266. doi:10.1016/j.epsl.2010.12.028

Neukum G (1983) Meteoritenbombardement und datierung planetarer oberflachen, Habilitation Dissertation for Faculty Membership. Ludwig-Maximilians-University, Munich

Neukum G, Ivanov B, Hartmann W (2001) Cratering records in the inner solar system in relation to the lunar reference system. Space Sci Rev 96:55–86. doi:10.1023/A:1011989004263

Ono T, Kumamoto A, Nakagawa H, Yamaguchi Y, Oshigami S, Yamaji A, Kobayashi T, Kasahara Y, Oya H (2009) Lunar radar sounder observations of subsurface layers under the nearside maria of the Moon. Science 323:909–912. doi:10.1023/A:1011989004263

Ohtake M, J Haruyama T, Matsunaga Y, Yokota T, Morota C, Honda, LISM Working Group (2008) Performance and scientific objectives of the SELENE (KAGUYA) Multiband Imager. Earth Planet Space 60:257–264

Ohtake M, Matsunaga T, Yokota Y, Yamamoto S, Ogawa Y, Morota T, Honda C, Haruyama J, Kitazato K, Takeda H, Iwasaki A, Nakamura R, Hiroi T, Kodama S, Otake H (2010) Deriving the absolute reflectance of lunar surface using SELENE (Kaguya) multiband imager data. Space Sci Rev 154:57–77. doi:10.1007/s11214-010-9689-0

Otake H, Ohtake M, Hirata N (2012) Lunar iron and titanium abundance algorithms based on SELENE (Kaguya) multiband imager data. In: Proceedings of the 43rd lunar science conference, No. 1905. doi:10.1023/A:1011989004263

Pieters CM (1978) Mare basalt types on the front side of the Moon—a summary of spectral reflectance data. In: Lunar 9th planetary conference, pp 2825–2849

Pieters CM, Head JW III, Adams JB, McCord TB, Zisk SH, Whitford-Stark JL (1980) Late high-titanium basalts of the western maria: geology of the flamsteed region of Oceanus Procellarum. J Geophys Res 85:3913–3938

Pike RJ (1977) Size-dependence in the shape of flesh impact craters on the Moon. In: Roddy DJ, Pepin RO, Merrill RB (eds) Impact and explosion cratering. Pergamon Press, New York, pp 489–509

Pritchard ME, Stevenson DJ (2000) Thermal aspects of a lunar origin by giant impact. In: Canup R, Righter K (eds) Origin of the Earth and Moon. University of Arizona Press, pp. 179–196

Qiao L, Xiao L, Zhao J, Huang Q, Haruyama J (2014) Geological features and evolution history of Sinus Iridum, the Moon. Planet Space Sci 101:37–52

Qiu J, Stone R (2013) Chinese Mission Ushers in new era of lunar exploration. Science 342:1026

Robinson MS, Brylow SM, Tschimmel M, Humm D, Lawrence SJ, Thomas PC, Denevi BW, Bowman-Cisneros E, Zerr J, Ravine MA, Caplinger MA, Ghaemi FT, Schaffner JA, Malin MC, Mahanti P, Bartels A, Anderson J, Tran TN, Eliason EM, McEwen AS, Turtle E, Jolliff BL, Hiesinger H (2010) Lunar reconnaissance orbiter camera (LROC) instrument overview. Space Sci Rev 150:81–124. doi:10.1007/s11214-010-9634-2

Schaber GG (1969) Geologic map of the Sinus Iridum quadrangle of the Moon. Rep., U.S. Geological Survey, Tech

Schaber GG (1973) Lava flows Mare Imbrium: geologic evaluation from Apollo orbital photography. In: Proceedings of the 4th lunar science conference, pp 73–92

Siegler MA, Smrekar SE (2014) Lunar heat flow: regional prospective of the Apollo landing sites. J Geophys Res 119:47–63

Solomon SC, Chaiken J (1976) Thermal expansion and thermal stress in the Moon and terrestrial planets: clues to early thermal history. In: Proceedings of the 7th lunarar science conference, pp 3229–3243

Solomon SC, Head JW (1979) Vertical movement in mare basins: relation to mare emplacement, basin tectonics, and lunar thermal history. J Geophys Res 84:1667–1682

Solomon SC, Head JW (1980) Lunar mascon basins: lava filling, tectonics, and evolution of the lithosphere. Rev Geophys 18:107–141. doi:10.1029/RG018i001p00107

Spudis PD, Hawke BR, Lucey PG (1988) Materials and formation of the Imbrium basin. In: Proceedings of the lunar and planetary science conference, vol 18, pp 155–168

Spudis PD (1993) The geology of multi-ring impact basins. Cambridge University Press, Cambridge

Thiessen F, Besse S, Staid MI, Hiesinger H (2014) Mapping lunar mare basalt units in mare Imbrium as observed with the Moon Mineralogy Mapper (M3). Planet Space Sci 104:244–252. doi:10.1016/j.pss.2014.10.003

Twiss RJ, Moores EM (2006) Structural geology, 2nd edn. W. H Freeman and Company, New York

Wagner R, Head JW III, Wolf U, Neukum G (2002) Stratigraphic sequence and ages of volcanic units in the Gruithuisen region of the Moon. J Geophys Res 107

Watters TR, Robinson MS, Beyer RA, Banks ME, Bell JF, Pritchard ME, Hiesinger H, van der Bogert CH, Thomas PC, Turtle EP, Williams NR (2010) Evidence of recent thrust faulting on the Moon revealed by the lunar reconnaissance orbiter camera. Science 329:936–940. doi:10.1126/science.1189590

Watters TR, Robinson MS, Banks ME, Tran T, Denevi BW (2012) Recent extensional tectonics on the Moon revealed by the lunar reconnaissance orbiter camera. Nature Geosci 5:181–185. doi:10.1038/ngeo1387

Watters TR, Robinson MS, Collins GC, Banks ME, Daud K, Williams NR, Selvans MM (2015) Global thrust faulting on the Moon and the influence of tidal stresses. Geology 43:851–854. doi:10.1130/G37120.1

Wilhelms DE, McCauley J (1971) Geologic map of the near side of the Moon, USGS Map I–703, scale 1:5,000,000

Williams GE (2000) Geological constraints on the Precambrian history of Earth's rotation and the Moon's orbit. Rev Geophys 38:37–59. doi:10.1029/1999RG900016

Williams KK, Zuber MT (1998) Measurement and analysis of lunar basin depths from Clementine altimetry. Icarus 131:107–122. doi:10.1006/icar.1997.5856

Williams NR, Watters TR, Pritchard ME, Banks ME, Bell JF III (2013) Fault dislocation modeled structure of lobate scarps from Lunar Reconnaissance Orbiter Camera digital terrain models. J Geophys Res Planets 118:224–233. doi:10.1002/jgre.20051

Whitaker EA (1972) Lunar color boundaries and their relationship to topographic features: a preliminary survey. Moon 4:348–355. doi:10.1007/BF00562002

Wöhler C, Lena R, Geologic Lunar Research (GLR) Group (2009) Lunar intrusive domes: morphometric and analysis and laccolith modeling. Icarus 204:381–398. doi:10.1016/j.icarus.2009.07.031

Young RA (1976) The morphological evolution of mare-highland contacts: a potential measure of relative mare surface age. In: Proceedings of the 7th lunar science conference, pp 2801–2816